ToF-SIMS Single Beam Depth Profiling and Ion Beam-Induced Hydrophobic Patterning of a Nanoporous Gold Absorber for Decay Energy Spectrometry

Shin Muramoto[1] (0000-0003-3135-375X), Mike Verkouteren[1] (0000-0002-5155-9926), Adam Pearce[2] (0000-0003-1068-703X), Ryan Fitzgerald[2] (0000-0002-0993-1085), Denis E. Bergeron[2] (0000-0003-1150-7950)

[1]Materials Measurement Sciences Division, National Institute of Standards and Technology, Gaithersburg, MD 20899

[2]Radiation Physics Division, National Institute of Standards and Technology, Gaithersburg, MD 20899

Corresponding author:
Shin Muramoto
National Institute of Standards and Technology, Gaithersburg, MD 20899
1-301-975-5997 (phone)
1-301-417-1321 (fax)
simuramoto@gmail.com

For publication in: Surface and Interface Analysis

Abstract

Decay energy spectroscopy relies on the absorber, a small substrate where the radioisotopes are embedded and thermalized, for high counting efficiency and spectroscopic energy resolution. This absorber in the form of a nanoporous Au was manufactured to prevent the formation of large crystals containing the radionuclides and other impurities that can result in degraded energy resolution and complex spectral artifacts. In this work, advanced surface analytical tools were used to validate the performance of the 2.5 µm nanoporous Au absorber. The chemical composition of the alloy was successfully determined to be 99 % Au after acid etching using x-ray photoelectron spectroscopy (XPS), formation of the nanoporous structure was visualized using scanning electron microscopy (SEM) and focused ion beam (FIB) to have <100 nm pores with a void space of (38 ± 14) %, and most importantly, time-of-flight secondary ion mass spectrometry (ToF-SIMS) operated in single beam depth profiling was demonstrated for the first time to be an effective method for measuring the transfer and embedding of radionuclides within the Au nanoporous matrix. Some ion bombardment induced artifacts were seen, but the effect was modest and not critical for the visualization of solute into the nanoporous matrix. It was also demonstrated that hydrophobic patterning could be produced on the nanoporous matrix using the equipped ion beam to prevent solution overflow, which was an important quality given that miniaturization of the absorber (e.g., less than 2 mm x 2 mm) was associated with increased signal to noise and reduced tailing.

Key words: nanoporous gold, decay energy spectrometry, ToF-SIMS, single beam depth profiling

Introduction

Measurements of radionuclide activity are essential for applications across nuclear security, environmental monitoring, and medicine. Traditional methods for primary standardization of activity typically rely on multi-step processes, such as absolute counting using a liquid scintillation-based method[1, 2] combined with separate spectroscopic purity analysis (e.g., gamma-ray spectrometry or mass spectrometry),[3] and are often limited to high-purity, single-radionuclide solutions due to potential isobaric contributions from impurities and decay products. To overcome these limitations, researchers at the National Institute of Standards and Technology (NIST) are refining the decay-energy spectrometry (DES) into a primary metrological tool for absolute massic activity measurements.[4-6] These applications utilize ultralow-temperature sensors, such as transition edge sensors (TES) and magnetic microcalorimeters (MMC), to measure very small amounts of thermal energy such as the energy of an incident x-ray photon (≈ 1 pJ).[7, 8] While both technologies offer the extreme sensitivity required for high-resolution metrology such as nuclear dating,[9] nuclear spectrometry,[10, 11] and activity measurements,[12-14] this work focuses on the TES, which leverages the ultra-narrow phase transition between superconducting and non-superconducting states, where the resistance of a TES becomes extremely sensitive to very small changes in temperature.[8 15] The goal for DES at NIST is to be able to measure alpha and beta decays and correlate activity with mass (activity concentration in units of Bq/g of radioactive solution),[6] achieving high counting efficiency for quantification and spectroscopic resolution for radionuclide identification in a single measurement.

Critical to achieving the DES goal is the absorber, a small substrate where the radioisotopes are embedded and thermalized, ensuring the 4π geometric efficiency necessary to achieve 100 % counting efficiency for alpha- and beta-emitting radionuclides. A significant challenge in source preparation is the creation of the radioactive sample itself, where the drying of the aqueous radionuclide solution often leads to the formation of large salt crystals and accumulation of non-volatile residues that can dampen the energy from decay particles,[7] resulting in degraded energy resolution and complex spectral artifacts.[6] The nanoporous Au,[16, 17] for example, has been used to address this issue.[10] In addition to its excellent thermalization properties,[18, 19] the high surface area and porous volume of the nanoporous matrix allows increased sample loading and controlled embedding of the radionuclide, which can lead to enhanced energy resolution by capturing nearly all of the decay energy in the absorber foil. However, a rigorous characterization of the nanoporous film is required to validate its performance and reproducibility for metrological use.

In this work, we confirm the chemical composition of the alloy using x-ray photoelectron spectroscopy (XPS), verify the formation of the nanoporous structure using scanning electron microscopy (SEM), and focused ion beam (FIB) milling to visualize the extent of pore formation

using cross-sectional analysis. We investigate the crucial aspect of liquid penetration using water contact angle measurements to verify the effective wicking of the aqueous solution into the porous volume. Finally, we use time-of-flight secondary ion mass spectrometry (ToF-SIMS) to obtain a depth profile of a tracer ion into the film, providing evidence that the analytes were successfully distributed within the porous matrix. Although depth profiles of porous matrices have been reported,[20] the use of a single beam for analysis and sputtering of a noble metal using this instrument has not been performed to date. Additionally, hydrophobic patterns on the absorber surface were implemented to constrain the deposit of the radionuclide solution, important especially in cases where the deposition of very large droplets must be achieved on a small absorber surface to prevent overflow and potential loss of material. These results were indispensable for establishing the nanoporous gold film as a viable and optimized absorber material for next-generation DES microcalorimetry.

Experiment

Sample Preparation. 10 cm Si(100) wafers purchased from Virginia Semiconductors[1] (Fredericksburg, VA) were diced into 15 mm × 15 mm square pieces using the Disco DAD341 dicing saw (Tokyo, Japan) equipped with a 15 µm diamond impregnated metal blade. 30 µm thick gold foils were purchased from Goodfellow (Pittsburgh, PA) and used as received. Individual specimens were soaked overnight in ultrapure water to remove salts, and sonicated sequentially for 10 min in acetone and methanol to remove organic contaminants. Roughly 100 nm of Au was deposited onto the Si substrate with a 10 nm Ti adhesion layer using a sputter deposition system (Denton Discovery 550, Moorestown, NJ) with deposition rates of approximately 0.43 nm/s and 0.17 nm/s, respectively, and a sample rotation speed of 3 rad/s to minimize circular variation. On top of the Au layer, roughly 2.5 µm film of the Au and Ag alloy was co-sputtered at rates of 0.43 nm/s and 0.62 nm/s, respectively, for a target Au atomic fraction of roughly 40 % to 50 %, which is shown to be optimal for nanoporous formation.[21, 22] The resulting films were left overnight in 14.4 mol/dm^3 HNO_3 solution for de-alloying (≈ 16 h), where the Ag formed a nitrate and dissolved away to leave a nanoporous structure. Hydrophobic surfaces, where needed, were prepared using a 4 mmol/dm^3 solution of dodecane in ethanol and vapor deposited inside a plastic desiccator using house vacuum for 1 h. Cesium nitrate was initially chosen as a tracer to visualize solute transfer within the nanoporous matrix, dissolved in ultrapure water to a concentration of 0.05 µg/g. A Europium (III) chloride hexahydrate, used as a non-radioactive surrogate for trivalent actinides, was heated at 120 °C

[1] Certain commercial equipment, instruments, or materials are identified in this paper to adequately specify the experimental procedure. Such identification does not imply recommendation or endorsement by the National Institute of Standards and Technology, nor does it imply that the materials or equipment identified are necessarily the best available for the purpose.

for 24 h to form an anhydrous salt, then dissolved in 1 mol/dm^3 nitric acid solution to a concentration of 0.66 μg/g. These were deposited using a Jet Lab 4 (MicroFab, Plano, TX) piezoelectric drop-on-demand printer system equipped with a 50 μm ID orifice print head, using a sinusoidal wave form with a peak voltage of 37 V and a period of 79 μs. For the Cs solution, 16,600 drops with a mass of (60.2 ± 0.4) ng per drop was used. For the Eu solution, 500 drops with a mass of (86.7 ± 0.4) ng per drop were printed onto various locations, yielding a deposit of roughly 0.028 ng of Eu per deposit, which is comparable to the actual amount of actinide used in recent DES experiments at NIST.[5] All samples were stored at room temperature and analyzed within 5 days of production.

Sample Analysis. X-ray photoelectron spectroscopy (XPS) measurements were made using the Kratos Axis Ultra (Kratos Analytical, Manchester, UK) using a monochromatic Al K_α source with an emission of 10 mA and anode bias of 15 kV. Survey scans were made using a pass energy of 160 eV with 1 eV energy resolution. Scanning electron microscopy (SEM) images of the crater topography were acquired using a JSM 7800 (Jeol, Tokyo, Japan) with an incident electron energy of 2 keV for analyzing the outermost morphology of the surface features using the standard Everhart-Thornley detector (ETD). Working distance was held at around 8 mm to enhance topographical contrast. A cross section of the nanoporous Au was prepared using the Helios Nanolab 660 (FEI, Portland, OR) focused ion beam (FIB) with a 30 keV Ga source over a platinum protection layer. ToF-SIMS depth profiles were performed using an IONTOF IV (Münster, Germany) equipped with a 30 keV Bi_3^+ liquid metal ion source and a 20 keV $Ar_{2600\pm1000}^+$ gas cluster ion beam (GCIB) for sputtering. Given that the gas cluster source provides low sputtering yields of heavy metals such as gold,[23] the nanoporous substrate was depth profiled in the single beam mode using Bi_3^+, where pulsed ions were used for analysis and direct current beam was used for sputtering. 500 μm × 500 μm craters were formed with 50 scans of analysis and 110 scans of sputtering per cycle, where the corresponding ion fluences were 2.5×10^{10} cm^{-2} (0.12 pA) and 4.5×10^{14} cm^{-2} (1.0 nA), respectively. The gas cluster source was used primarily for etching away the organic film for hydrophobic patterning, where 1 mm × 1 mm areas were etched away at (50, 100, 200, 300, and 500) scans per spot, equal to ion fluences of (0.275, 0.550, 1.10, 1.65, and 2.75) × 10^{15} cm^{-2}, respectively. Crater depth and topography measurements were performed using a Dektak XT stylus profilometer (Bruker Corporation, Tucson, AZ) equipped with a 2.5 μm radius stylus tip, having a vertical resolution of 6 nm. A 2 mm line scan was used to ensure that a large enough region outside the crater was measured to provide sufficient area for leveling. For all analyses, values are averages of at least three measurements and the stated uncertainty represents the standard deviation unless otherwise noted.

Results and Discussion

Characterization of nanoporous gold. Chemical composition of the nanoporous film before and after de-alloying was measured using XPS. Directly after deposition, the Au atomic fraction varied from (40 to 52) % from the center to the edge of the wafer holder (Figure 1). Due to the horizontally opposed orientation of the Au and Ag targets inside the deposition chamber, the lighter Ag ions may have scattered in flight and led to differences in the observed composition. De-alloying the ≈ 43 % Au films at an acid concentration of 14.4 mol/dm^3 for (1, 6, and 16) h led to Au atomic fractions of (90, 94, and 99) %, respectively, showing the speed of Ag removal. However, since the XPS information depth is limited to tens of nanometers, the longer exposure time of 16 h was chosen to ensure that the subsurface region of the film was also de-alloyed.

De-alloying of the film was confirmed visually, where in Figure 2 the aerial and cross-sectional electron micrographs showed the surface and sub-surface regions of the porous matrix, respectively. On the surface, the shorter etching time was associated with the formation of a coarse, granular morphology with clusters of irregular pores. With extended etching, this was seen to evolve into a nanoporous sponge-like structure where both solid and void phases were more uniform throughout. Cross-sectional analysis revealed a uniform interconnected structure that extended to the substrate interface, which indicated a successful penetration of the acid into the subsurface region. A few elongated openings were seen, but this was due to cracks forming in the film, where one of them can be seen in the aerial image. In addition, the Si substrate appeared mechanically stable and showed no signs of delamination, which was a result of the ≈ 100 nm Au layer that prevented the acid from oxidizing the Ti adhesion layer (or the Si substrate). Calculation of the pore size using an imaging software estimated the void space to be roughly (38 ± 14) %, where the large uncertainty reflected the variability in morphology across multiple films.

The corrugated appearance of the Si substrate was a focused ion beam (FIB) artifact called curtaining.[24, 25] The nanoscale morphology of the matrix presented variable local angles with respect to the incident ion beam, leading to angle-dependent variations in the local sputter yield, and this was seen to transfer into the substrate.

Verification of volumetric solute transfer using single beam depth profiling. Figure 3a shows the optical micrograph of a 1 µL droplet as it was absorbed into the nanoporous substrate. Roughly 16,000 drops of picoliter-sized drops were deposited, forcing the footprint to expand to roughly 3.7 mm diameter as the liquid wicked into the matrix. After a short time, the footprint was seen to become constant, and the liquid deposit started to decrease in volume as shown. To verify and to visualize the extent of Cs transfer into the pores of the matrix, ToF-SIMS was used to visualize its distribution both vertically as well as laterally within the subsurface region. Another possible approach to visualizing the distribution is to image the film cross-section seen

in Figure 2. This approach would minimize ion bombardment artifacts such as interface broadening that could result in distortion of the true analyte distribution. However, given the relatively low useful yield of approximately 10^{-6} for preformed ions,[26] the very dilute concentration of Cs atoms delivered to the matrix meant that there would not be enough ions produced from the surface of the cross-section for detection. Figures 3c, 3d, and 3e show the lateral distributions of the Cs^+ ion as a function of sputtered depth, which showed the transition from a continuous layer to a heterogeneous distribution within the pores. At the surface, the Cs^+ signal appeared uniform and indicated a continuous deposit, with evidence of minor surface migration around the edge. In the sub-surface region, the distribution is more heterogenous, and Cs^+ concentration appeared highest within discrete locations that resembled pores and cracks within the matrix. At depths closest to the Si interface, the ions remain confined within these pores, confirming that the Cs atoms have fully penetrated into the porous structure. Interestingly, no migration outside of the deposit edge was seen, which suggested that once the deposit footprint is established, any remaining solute (as seen in Figure 3a) is forced to migrate vertically through the pores but not laterally beyond the edge. The reason for the apparent decrease in intensity with sputtered depth may be due to the lack of sensitivity in imaging mode for very small amount of material since the pore size is below the instrument's lateral resolution. Nonetheless, the Cs^+ ion profile in Figure 3f, which sums the intensity across all pixels for each scan, showed that the Cs^+ intensity remained relatively stable through the bulk of the film, which again confirmed the transfer of Cs atoms into the matrix. The initial transient region of the profile (i.e., surface layer down to about 250 nm) showed a rapid decrease in intensity but this was mostly an instrument artifact. Most profiles show rapid declines initially due to rapid changes in surface chemistry, such as from the implantation of the analysis ions that changes the surface work function as well as sputtering of adsorbates such as contaminants and salts that may enhance or attenuate ionization probability.

Within the steady state or the bulk region of the profile, the gentle decrease in Cs^+ intensity is attributed to progressive crater bottom roughening with depth. The primary driver of this significant topographical development is the growth of micron-sized pillars from masked sputtering.[27, 28] This mechanism is initiated at localized regions on the nanoporous surface where specific local incidence angles yield exceptionally low sputter yields. Profilometer measurements showed that the pillar heights were less than half the crater depth, which supports the mechanism of formation as masked sputtering and not deposition or growth. As can be seen in Figure 4, the pillars were non-uniform in spatial and size distributions, which meant that their formation was random and once formed, could not be removed due to the presence of angles that produced minimum sputter yields (e.g., angles parallel to the incident ion beam). The number density of pillars increased with sputtered depth, which progressively decreased the signal and the interface sharpness of the profile.

This broadening effect at the interface was substantial. The full width at half maximum (FWHM) of the Ti^+ substrate signal ((10 nm adhesion layer) was approximately 710 nm, and the depth resolution (ΔZ) of the Cs^+ profile was calculated to be 540 nm using the (84 – 16) % method. Beyond micropillar formation, this most likely includes contributions from atomic mixing as well as redeposition. These effects collectively distort the true depth distribution of the analyte. Consequently, while the Cs^+ signal is detected deep into the interface region, the data strictly supports volumetric penetration within the nanoporous matrix, rather than true penetration to the substrate interface.

For ultrathick films (i.e., > 2 µm),[27, 29] literature references lack direct comparisons for roughness and depth resolution scaling. However, Seah et al.[30] demonstrated that depth resolution can be approximated using a power law of the form $\Delta Z = aZ^{0.5}$ where a is a proportionality factor accounting for instrumental factors, initial film roughness, and cascade mixing. The authors note that a can vary from 0.1 to 10 depending on initial topography. Given the inherently high roughness of the nanoporous matrix, assigning a worst-case value of a = 10 yields a predicted ΔZ of 500 nm at a depth of Z = 2500 nm. This theoretical broadening closely matches our experimental measurement of 540 nm. While this artifact-driven broadening prevents us from definitively proving analyte penetration down into the substrate interface, it does not rule it out. This is discussed further in the following section, where the profile is compared to a control surface with no analyte penetration.

Hydrophobic patterning for controlled deposition and Europium as radionuclide surrogate. As discussed, the gold absorber converts the kinetic energy of radionuclide decay into a measurable thermal signal. While the nanoporous matrix can effectively mitigate energy scattering and damping by minimizing the formation of salt crystals or impurities,[7] spectral resolution such as peak broadening and low-energy tailing remain sensitive to the absorber's size (i.e., total heat capacity). Although minimizing the absorber volume to a footprint below 2 mm × 2 mm is ideal, this miniaturization complicates the deposition of the sample. Precise deposition using the inkjet printer becomes difficult, and the deposition of relatively high volume of dilute source solution have historically led to overflow. To overcome this, hydrophobic patterning was employed to guide and constrain the liquid deposit, ensuring localized containment as the solution wicked into and dried within the matrix. This was done by vapor deposition of an alkanethiol followed by the argon gas cluster sputtering, known for its ability to remove organic layers much faster than inorganic ones given its low energy per atom arrangement.[31, 32] On a side note, extended exposure of the nanoporous Au to atmosphere resulted in a hydrophobic surface due to the adsorption of adventitious carbon, therefore using the alkanethiol was a better controlled approach for preparing a similarly behaving surface.

Figure 5a shows an array of the miniature Au absorbers and how they aligned with the print head. In this particular example, although the printhead was aligned with the center of the sputtered area in Figure 5b, the deposit landed in the hydrophobic area due to some charge induced deflection but was found to quickly migrate to the sputtered, hydrophilic area. In addition, a very large volume of solution could be contained within that area and not result in overflow or migration of the deposit (data not shown). Contact angle measurements of the areas showed that the sputtered region was significantly more hydrophilic, with the SEM images showing intact nanoporous morphology even after 2.75×10^{15} cm^{-2} of GCIB sputtering to remove the alkanethiol film.

To confirm the removal of the alkanethiol film in the sub-surface region and to verify the volumetric solute transfer into the matrix, a 1 mol/dm^3 HNO_3 solution of Eu was used as a non-radioactive surrogate for trivalent actinides, for which this matrix was designed. Instead of using Cs as in the previous section, the use of Eu would allow observations of how salts and impurities in an acidic solvent would behave on the porous matrix. Figure 6 shows the deposit of Eu on Si, where it was characterized by a coffee ring-type of residue, suggesting that there was a large amount of contamination in the solution which could potentially affect the transfer of decay energy. ToF-SIMS imaging revealed the presence of amines (nitrogen adducts) which suggested that nitric acid may have reacted with carbon impurities from the solvent, container, and/or the atmosphere to form non-volatile species. While the majority of these products were found in the ring, metals such as Na and Eu seemed to be distributed uniformly within the deposit.

Figures 7a and 7b show the same solution deposited on the hydrophobic and sputtered regions of the nanoporous Au, respectively. Interestingly, for both cases, the residue was characterized by the lack of a coffee ring, suggesting that there was transport of material into the cracks or the nanopores of the matrix despite the former having a hydrophobic coating that prevented liquid penetration. As can be seen in the images, the hydrophobic coating forced the droplet to have a much smaller footprint as it dried, which should have left a thicker residue but this was not readily apparent. ToF-SIMS images revealed faint coffee rings made of CNO^- on the hydrophobic surface, with the solvent fronts indicating migration of the deposit as it dried. This implied that the solute had settled into the void towards the final stages of drying. Conversely, the sputtered surface induced the deposit to spread and deposit the solute uniformly, presumably with the solute penetrating into the pores before drying. In either case, larger molecules such as $C_5H_{12}N^+$ were barely detectable on the surface, suggesting that these contaminants had settled into the pores and cracks and had become segregated enough to be below the detection threshold of the instrument. Smaller molecules and atoms such as CNO^- and Na^+ generally have higher ionization probabilities,[33] which made them likely to be more detectable at similar concentrations.

Figure 8 shows the result of single beam depth profiling in both regions, showing the intensity of Eu^+ as a function of depth. The depth profiles are constructed from 200 µm × 200 µm regions of interest, where Na^+ is highest in the hydrophobic surface (Figure 7d) and at center of the deposit in the sputtered surface (Figure 7f). Since the ionization potential of Eu is much higher compared to Cs (547 kJ/mol and 376 kJ/mol, respectively), Eu is more difficult to ionize and therefore imaging did not reveal much in terms of revealing spatial distribution. However, some signal could be obtained for depth profiling since the intensity was summed across all pixels. As can be seen in Figure 8, analysis of the hydrophobic surface was characterized by a rapid decay in intensity of Eu^+ in the transient region and a very low signal in the steady state region that continued into the substrate, suggesting that this is background noise. The rapid decay at the beginning indicates that the solute (including contaminants) are predominantly constrained at the surface, as expected. Conversely, the sputtered region also showed a sharp decline in the transient region but the steady state region was marked by a generally stable Eu^+ signal followed by decay as it reached the substrate. These results confirm that GCIB sputtering for the removal of the hydrophobic film was effective and the ion dose was sufficient for solute transfer to occur in the sub-surface region.

The measured FWHM of the Ti^+ adhesion layer was approximately 700 nm, suggesting a similar extent of interface broadening from instrument artifacts as observed in the Cs^+ profile. This broadening distorts the true distribution of the analyte, making it difficult to conclude whether penetration down into the substrate interface occurred. However, comparison with the control hydrophobic surface shows that the analyte penetrated a large fraction of the nanoporous matrix. Although depth distributions must be interpreted with caution given these instrument artifacts, the minimal subsurface tailing observed on the hydrophobic control indicates that the effect of cascade atomic mixing is not profound, at least at these depths. Therefore, while the precise extent of analyte penetration into the substrate interface remains inconclusive, this depth profiling technique was effective for visualizing ultra-trace solute transport into the bulk of the nanoporous matrix.

Conclusions

Advanced surface analytical tools were used to validate the manufacture and function of a novel nanoporous Au absorber for use in decay energy spectroscopy. The chemical composition of the alloy was successfully determined using XPS, formation of the nanoporous structure was visualized using SEM and FIB, and ToF-SIMS operated in single-beam depth profiling mode was demonstrated for the first time to be an effective method for measuring ultra-trace solute transfer within an inorganic nanoporous matrix. Ion bombardment artifacts such as micropillar formation and cascade atomic mixing, produced substantial interface broadening that obscured the true depth distribution of the solute closer to the interface. However, comparison with a hydrophobic control showed that this technique was effective for visualizing ultra-trace solute

transport into the bulk of the nanoporous matrix, although the precise extent of analyte penetration into and across the substrate interface remains unresolved. Future work will focus on the use of sample rotation[27, 34, 35] to reduce interface broadening. It was also demonstrated that GCIB could successfully be used to sputter away organic films while keeping the nanoporous morphology intact, an important quality especially for hydrophobic patterning where miniaturization of a DES absorber is associated with better spectral quality and overflow of the radionuclide solution needs to be prevented. ToF-SIMS was also instrumental in elucidating the lateral distribution of salts and metals on the nanoporous surface, which was a requirement for minimizing crystal formation during solution drying. These results showed that these advanced analytical tools were indispensable for confirming and validating the performance characteristics of the nanoporous gold matrix, and their use is expected to continue as we explore and further optimize absorber materials for next-generation DES microcalorimetry.

Acknowledgements

This work was supported in part by the National Institute of Standards and Technology (NIST) Innovations in Measurement Science (IMS) funding. Research was performed in part at the NIST Center for Nanoscale Science and Technology (CNST). Authors thank Max Carlson, Gordon Shaw, Dan Schmidt, and Galen O'Neil for valuable discussions.

Data Availability

Available upon request

Conflict of Interest

The authors declare no conflict of interest

Figure Captions

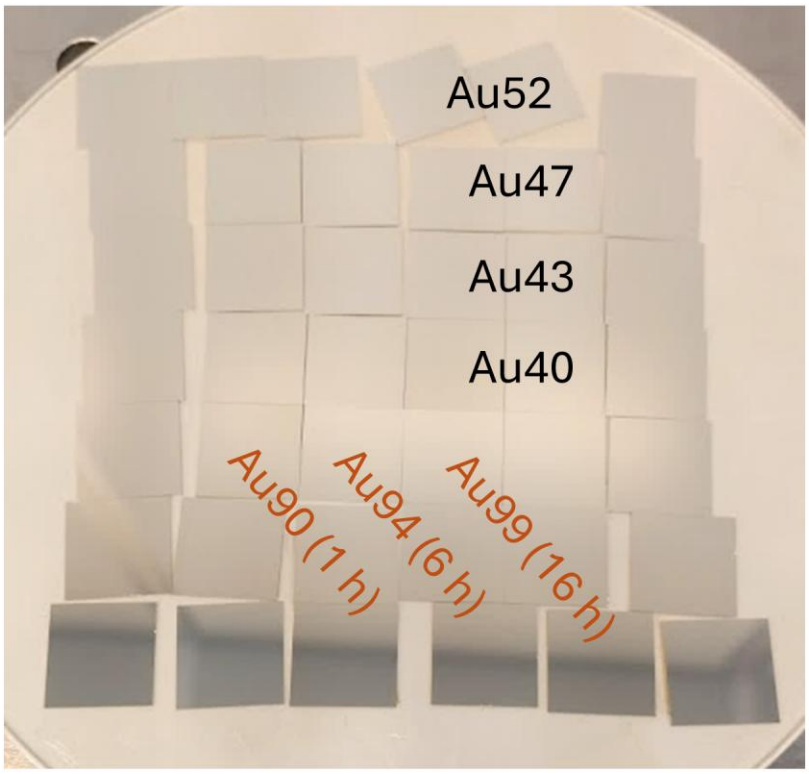

Figure 1. Optical micrograph showing an array of 15 mm × 15 mm Si pieces on a 150 mm wafer holder, before acid etching. The number (e.g., Au40) refers to the atomic fraction of Au as determined by XPS (balance is Ag, C 1s not included), with a trend towards higher Au fraction away from the center. It is not clear in the micrograph, but the center region had a slightly yellow-ish hue. The numbers in black and orange represent the Au fraction before and after acid etching, respectively, with the etching time in parentheses. The values are averages of 3 samples and the uncertainty was around 1%.

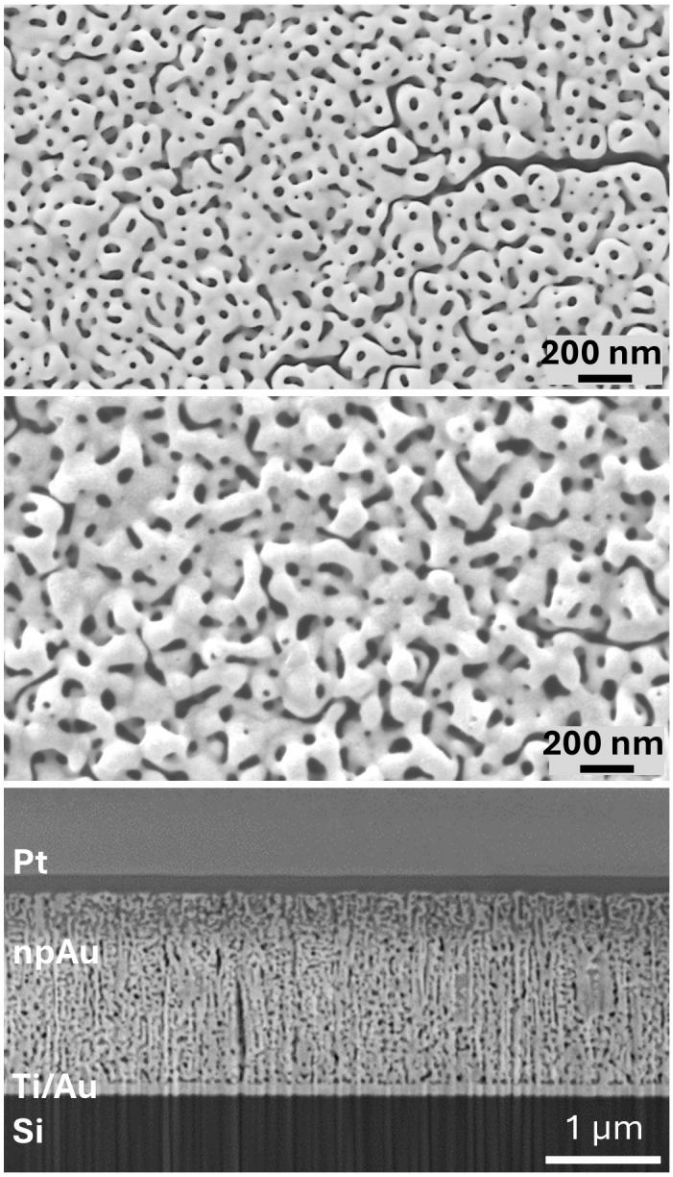

Figure 2. Scanning electron micrographs showing the porous structure of the surface after 6 h (top) and 16 h (center) of acid etching. The size marker is 200 nm. Bottom image shows the cross section of the 16 h etched film prepared using a FIB instrument. The layers from the top are: ≈ 1 µm Pt protection layer; ≈ 2.5 µm nanoporous Au layer; ≈ 100 nm Au layer; 10 nm Ti adhesion layer; and Si substrate.

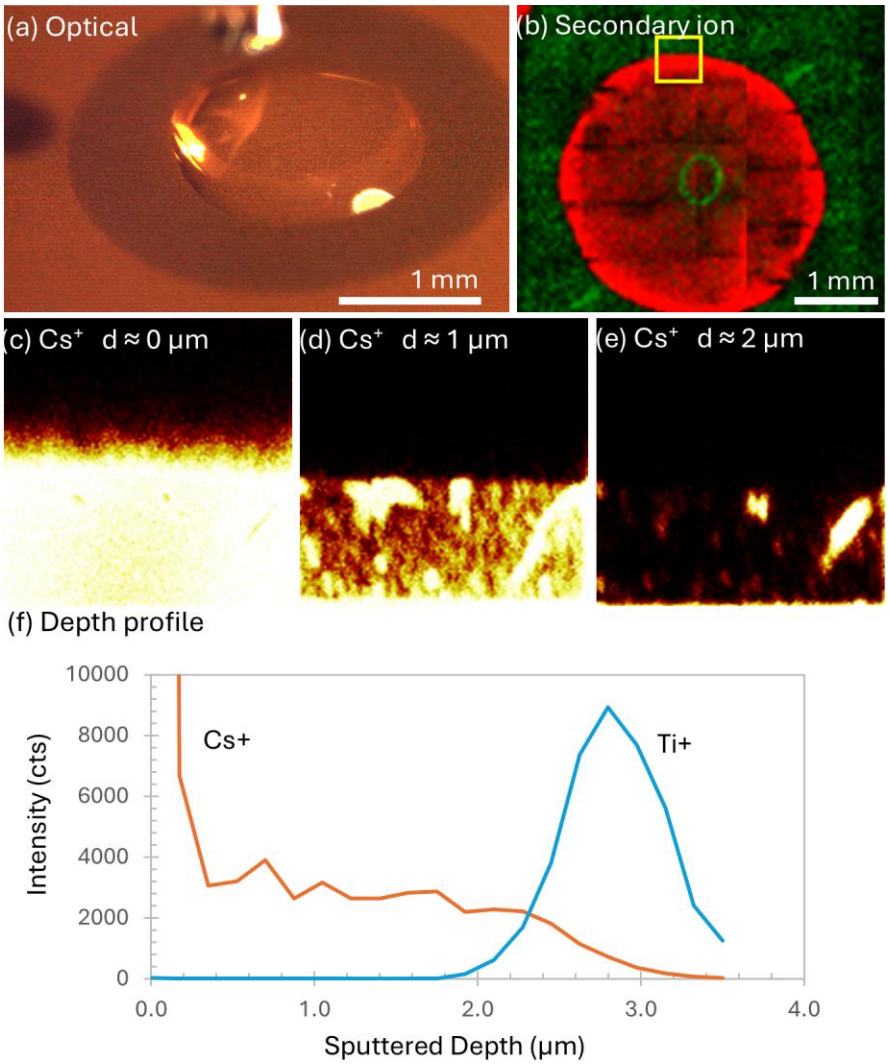

Figure 3. (a) Optical micrograph showing the 1 µL droplet as it is absorbed into the nanoporous substrate. 16,600 drops were deposited at 100 Hz, and the diameter of the wet footprint is roughly 3.7 mm. ToF-SIMS secondary ion images showing the lateral distribution of the Cs^+ ion (b) in the large map mode (green is Au^+), and as a function of sputtered depths at approximate depths of (c) 0 µm, (d) 1 µm, and (e) 2 µm. In (b), the yellow square is the analysis area from which images in (c), (d), and (e) were obtained. Brighter color denotes higher intensity. (f) ToF-SIMS depth profile showing the intensity of Cs^+ and Ti^+ as a function of depth.

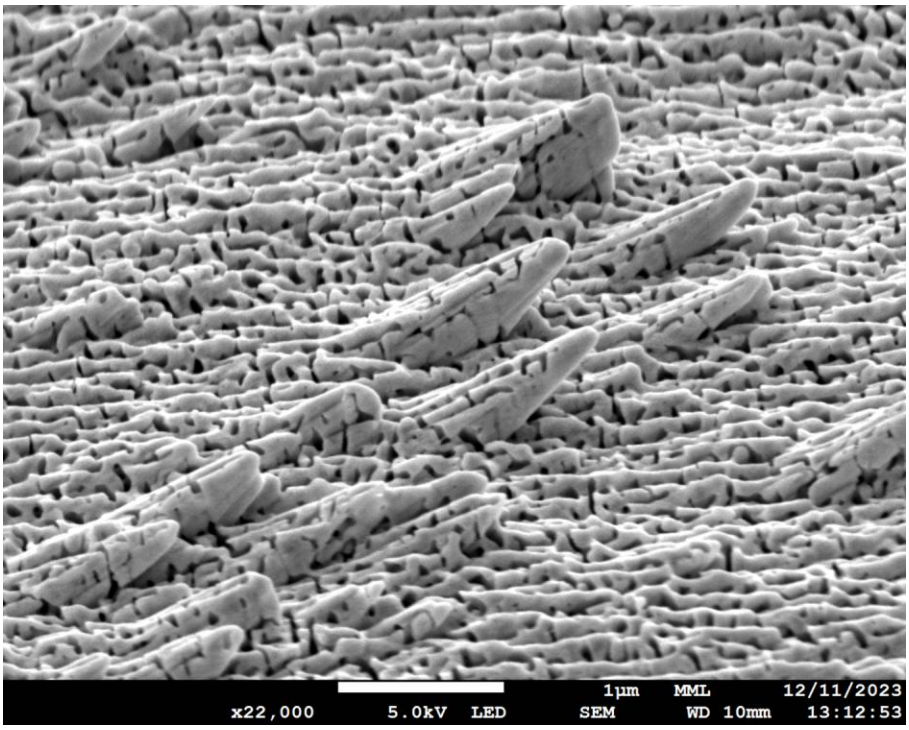

Figure 4. Secondary electron image at a tilted view (45°) showing the micropillars at the crater bottom within a sputtered region of 500 µm × 500 µm. Sputtering was performed using Bi in direct current mode with an ion fluence of roughly 5×10^{16} cm^{-2}. The ion beam is coming from the right at an angle of 45° with respect to the surface.

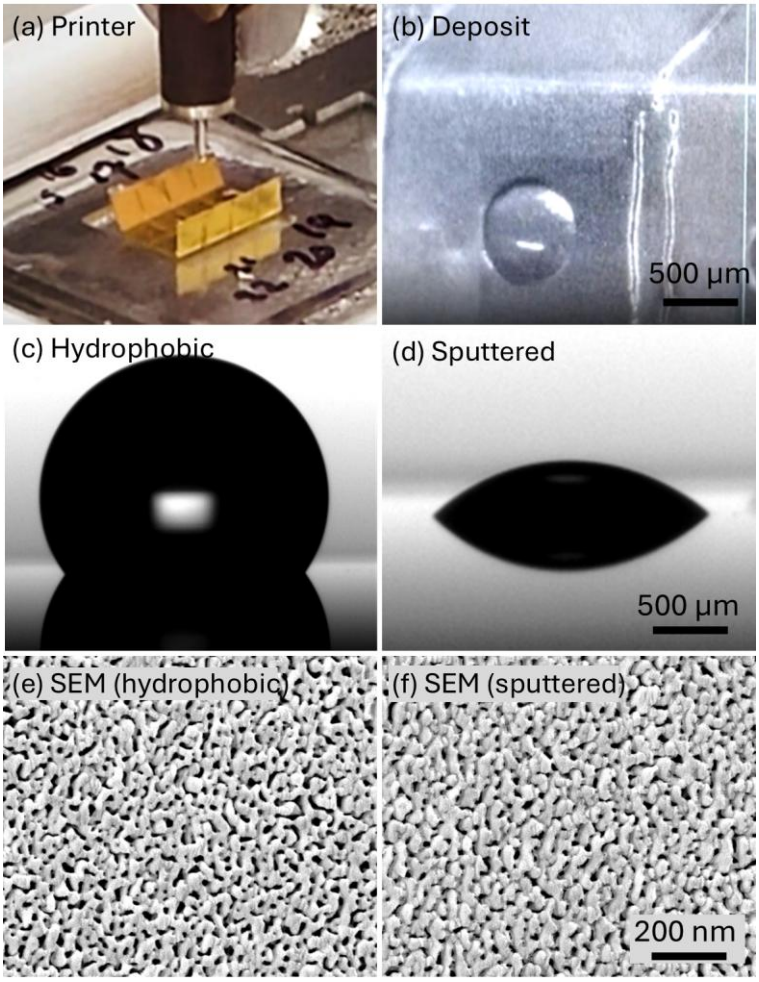

Figure 5. Optical micrographs showing (a) the inkjet print nozzle over an array of Au absorbers (each 2 mm × 4 mm) and (b) a ≈ 1000 pL deposit inside a 1 mm × 1 mm area etched within a hydrophobic layer. Contact angle measurements using 1 µL of ultrapure water performed on (c) a virgin hydrophobic layer (127°) and on (d) an area sputtered using GCIB (39°). Scanning electron micrographs showing the morphology of the nanoporous matrix (e) before and (f) after GCIB sputtering.

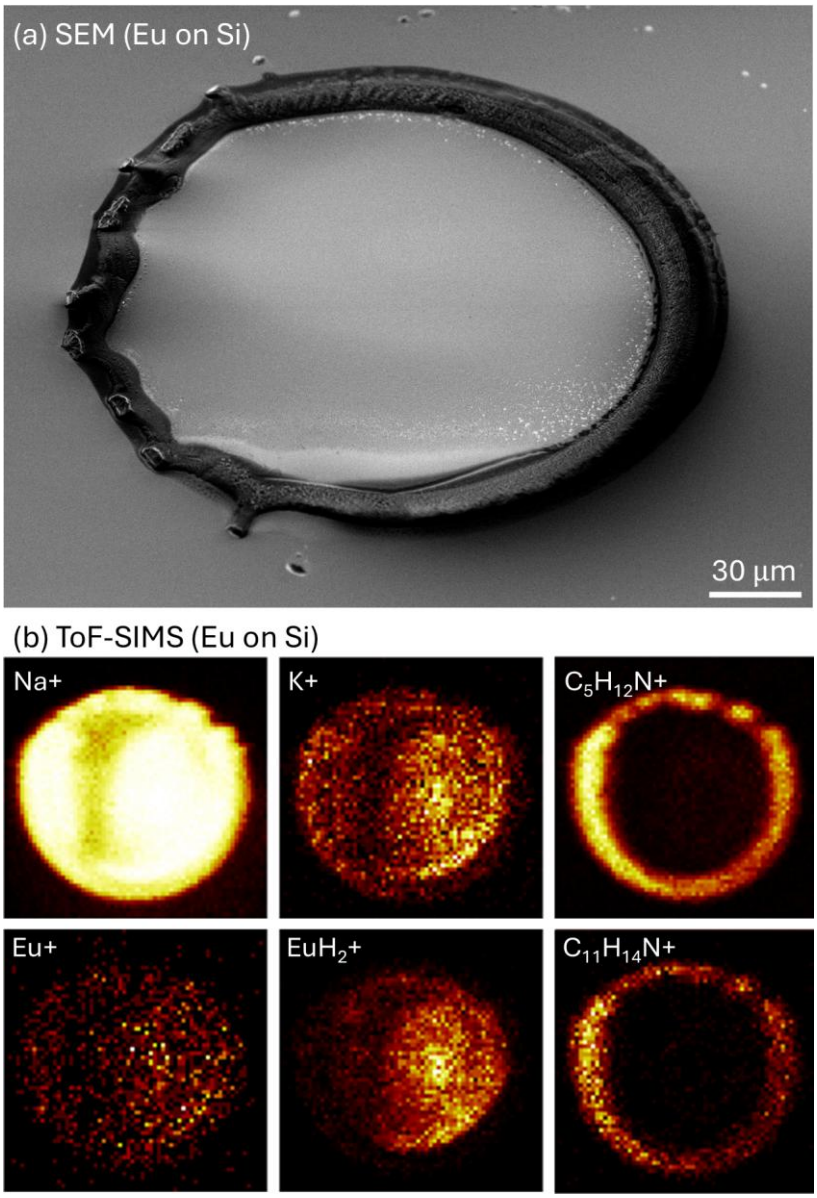

Figure 6. (a) Scanning electron micrograph showing the dried residue of the 500 drop EuCl solution inkjet-printed onto Si. (b) ToF-SIMS images showing the spatial distribution of respective secondary ions. Brighter color denotes higher intensity. Image size is 500 µm × 500 µm.

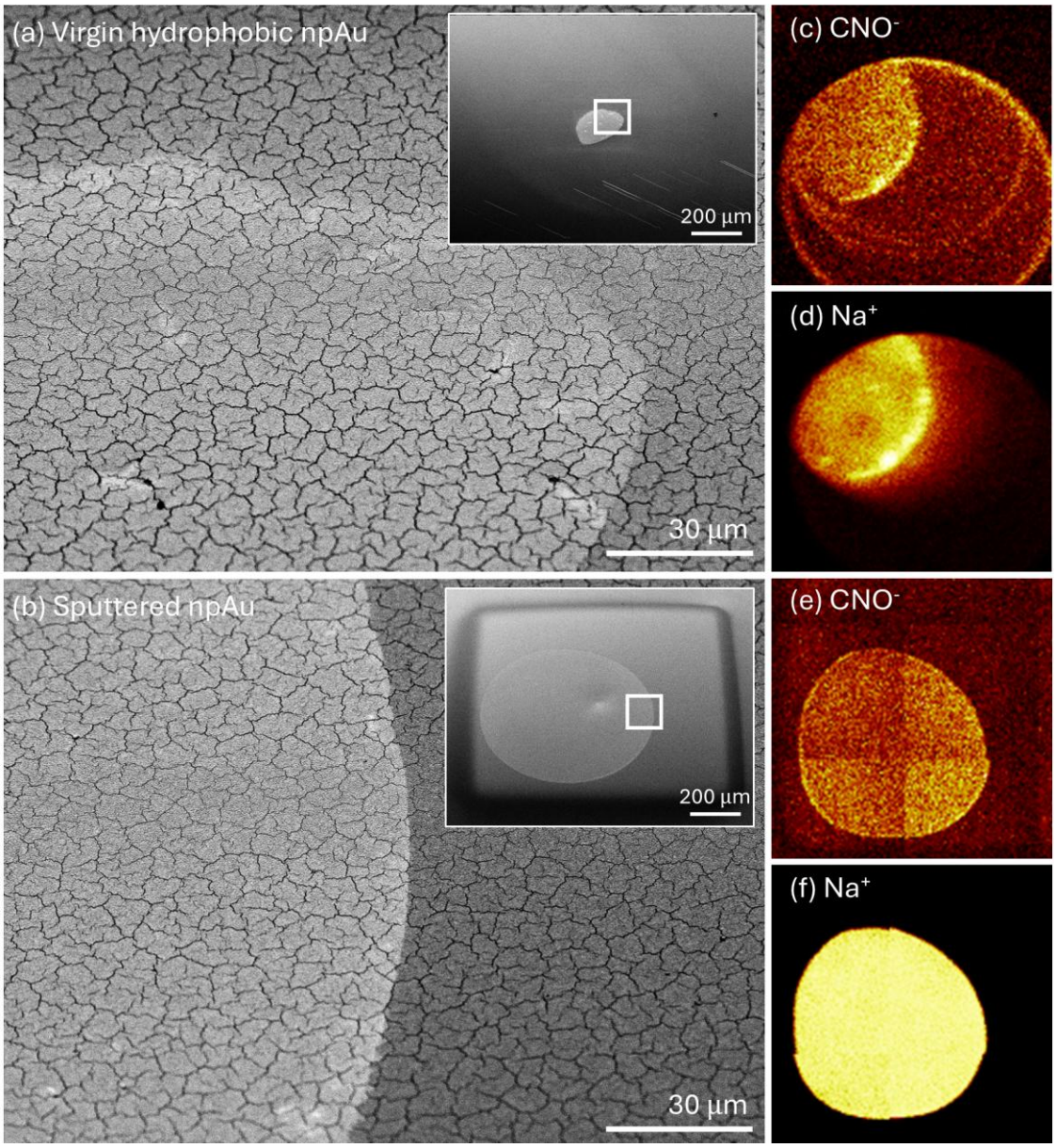

Figure 7. Scanning electron micrographs showing the dried residue of the 500 drop EuCl solution inkjet-printed onto (a) hydrophobic and (b) sputtered regions of the nanoporous Au, with the inset showing a less magnified view of the sputtered area, the deposit, and a square depicting the area from which the images were obtained. ToF-SIMS images show the spatial distribution of CNO^- and Na^+ ions on the hydrophobic (c, d) and sputtered (e, f) regions, respectively. In (c, d), the image size was 500 µm, and in (e, f), the image size was expanded to 1 mm to capture the entire deposit. SIMS is non-quantitative, therefore higher intensities in one image do not necessarily equate to higher number of atoms or molecules when compared to another image.

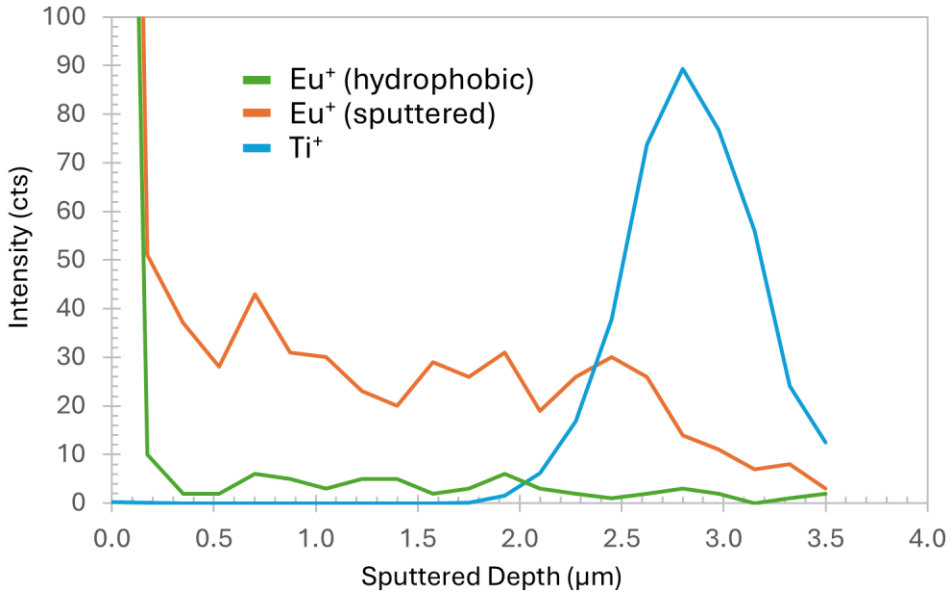

Figure 8. ToF-SIMS depth profile showing the intensities of Eu^+ deposited on the hydrophobic surface (hydrophobic), Eu^+ on the sputtered surface (sputtered), and Ti^+ as a function of depth. The sputter crater was 500 µm × 500 µm, and the depth profile was constructed from the center 200 µm × 200 µm region of interest. For both surfaces, the area in the center of the high Na^+ regions in Figures 7d and 7f were used for constructing the depth profile, respectively. The intensity of Ti^+ was reduced by a factor of 250 to fit the plot range.

References

(1) Broda, R.; Cassette, P.; Kossert, K. Radionuclide metrology using liquid scintillation counting. *Metrologia* **2007**, *44* (4), S36. DOI: 10.1088/0026-1394/44/4/S06.
(2) Kossert, K.; Broda, R.; Cassette, P.; Ratel, G.; Zimmerman, B. Uncertainty determination for activity measurements by means of the TDCR method and the CIEMAT/NIST efficiency tracing technique. *Metrologia* **2015**, *52* (3), S172. DOI: 10.1088/0026-1394/52/3/S172.
(3) Pommé, S. Methods for primary standardization of activity. *Metrologia* **2007**, *44* (4), S17. DOI: 10.1088/0026-1394/44/4/S03.
(4) Carlson, M.; Fitzgerald, R.; Schmidt, D.; O'Neil, G. Characterization of Transition Edge Sensors for Decay Energy Spectrometry. *J. Low Temp. Phys.* **2024**, *216* (1), 313–319. DOI: 10.1007/s10909-024-03135-9.
(5) Fitzgerald, R. P.; Alpert, B. K.; Bergeron, D. E.; Carlson, M.; Essex, R.; Jollota, S.; Morgan, K.; Muramoto, S.; Nour, S.; O'Neil, G.; et al. Primary activity measurement of an Am-241 solution using microgram inkjet gravimetry and decay energy spectrometry. *Metrologia* **2025**, *62* (4), 045005. DOI: 10.1088/1681-7575/adecaa.
(6) Fitzgerald, R. P.; Alpert, B. K.; Becker, D. T.; Bergeron, D. E.; Essex, R. M.; Morgan, K.; Nour, S.; O'Neil, G.; Schmidt, D. R.; Shaw, G. A.; et al. Toward a New Primary

Standardization of Radionuclide Massic Activity Using Microcalorimetry and Quantitative Milligram-Scale Samples. *J Res Natl Inst Stand Technol* **2021**, *126*, 126048. DOI: 10.6028/jres.126.048 From NLM.
(7) Kruse, S. J.; Scherrer, S. K.; Horne, G. P.; LaVerne, J. A.; Forbes, T. Z. The inorganic chemist's guide to actinide radiation chemistry: a review. *Inorganic Chemistry Frontiers* **2025**, *12* (21), 6398–6434, 10.1039/D5QI00975H. DOI: 10.1039/D5QI00975H.
(8) Irwin, K. D.; Hilton, G. C. Transition-Edge Sensors. In *Cryogenic Particle Detection*, Enss, C. Ed.; Springer Berlin Heidelberg, 2005; pp 63–150.
(9) Wood, R.; Kim, G.-b.; Jovanovic, I.; Lee, C.; Hines, N.; Parsons-Davis, T. Radioisotope dating of nuclear materials using cryogenic decay energy spectrometry. *J. Radioanal. Nucl. Chem.* **2026**. DOI: 10.1007/s10967-026-10742-1.
(10) Croce, M. P.; Rabin, M. W.; Mocko, V.; Kunde, G. J.; Birnbaum, E. R.; Bond, E. M.; Engle, J. W.; Hoover, A. S.; Nortier, F. M.; Pollington, A. D.; et al. Development of Holmium-163 Electron-Capture Spectroscopy with Transition-Edge Sensors. *J. Low Temp. Phys.* **2016**, *184* (3), 958–968. DOI: 10.1007/s10909-015-1451-2.
(11) Ullom, J. N.; Bennett, D. A. Review of superconducting transition-edge sensors for x-ray and gamma-ray spectroscopy*. *Superconductor Science and Technology* **2015**, *28* (8), 084003. DOI: 10.1088/0953-2048/28/8/084003.
(12) Kim, G. B.; Borg, L. E.; Boyd, S. T. P.; Cantor, R. H.; Despotopulos, J. D.; Drury, O. B.; Friedrich, S.; Gallant, A.; Hines, N. R.; Jacobs, A.; et al. Absolute Decay Counting of ^{146}Sm and ^{147}Sm for Early Solar System Chronology. *J. Low Temp. Phys.* **2022**, *209* (5), 824–831. DOI: 10.1007/s10909-022-02798-6.
(13) Müller, M.; Rodrigues, M.; Beyer, J.; Loidl, M.; Kempf, S. Magnetic Microcalorimeters for Primary Activity Standardization Within the EMPIR Project PrimA-LTD. *J. Low Temp. Phys.* **2024**, *214* (3), 263–271. DOI: 10.1007/s10909-024-03048-7.
(14) Tollefson, A. D.; Smith, C. M.; Carpenter, M. H.; Croce, M. P.; Fassbender, M. E.; Koehler, K. E.; Lilley, L. M.; O'Brien, E. M.; Schmidt, D. R.; Stein, B. W.; et al. Measurement of 227Ac impurity in 225Ac using decay energy spectroscopy. *Appl. Radiat. Isot.* **2021**, *172*, 109693. DOI: https://doi.org/10.1016/j.apradiso.2021.109693.
(15) Cabrera, B.; Clarke, R. M.; Colling, P.; Miller, A. J.; Nam, S.; Romani, R. W. Detection of single infrared, optical, and ultraviolet photons using superconducting transition edge sensors. *Appl. Phys. Lett.* **1998**, *73* (6), 735–737. DOI: 10.1063/1.121984 %J Applied Physics Letters (accessed 7/30/2025).
(16) Seker, E.; Reed, M. L.; Begley, M. R. Nanoporous Gold: Fabrication, Characterization, and Applications. *Materials* **2009**, *2* (4), 2188–2215.
(17) Ruffino, F.; Grimaldi, M. G. Nanoporous Gold-Based Sensing. *Coatings* **2020**, *10* (9), 899.
(18) Hopkins, P. E.; Serrano, J. R.; Phinney, L. M.; Li, H.; Misra, A. Boundary scattering effects during electron thermalization in nanoporous gold. *J. Appl. Phys.* **2011**, *109* (1). DOI: 10.1063/1.3530866 (accessed 2/4/2026).
(19) Ortolani, M.; Mancini, A.; Budweg, A.; Garoli, D.; Brida, D.; de Angelis, F. Pump-probe spectroscopy study of ultrafast temperature dynamics in nanoporous gold. *Physical Review B* **2019**, *99* (3), 035435. DOI: 10.1103/PhysRevB.99.035435.

(20) Lopez-Fontal, E.; Gin, S. Insights into Calcium Phosphate Formation Induced by the Dissolution of 45S5 Bioactive Glass. *ACS Biomaterials Science & Engineering* **2025**, *11* (2), 875–890. DOI: 10.1021/acsbiomaterials.4c01680.
(21) Dixon, M. C.; Daniel, T. A.; Hieda, M.; Smilgies, D. M.; Chan, M. H. W.; Allara, D. L. Preparation, Structure, and Optical Properties of Nanoporous Gold Thin Films. *Langmuir* **2007**, *23* (5), 2414–2422. DOI: 10.1021/la062313z.
(22) Kim, S. H. Nanoporous gold: Preparation and applications to catalysis and sensors. *Current Applied Physics* **2018**, *18* (7), 810–818. DOI: https://doi.org/10.1016/j.cap.2018.03.021.
(23) Matsuo, J.; Toyoda, N.; Akizuki, M.; Yamada, I. Sputtering of elemental metals by Ar cluster ions. *Nuclear Instruments and Methods in Physics Research Section B: Beam Interactions with Materials and Atoms* **1997**, *121* (1), 459–463. DOI: https://doi.org/10.1016/S0168-583X(96)00541-1.
(24) Zhong, X. L.; Haigh, S. J.; Zhou, X.; Withers, P. J. An in-situ method for protecting internal cracks/pores from ion beam damage and reducing curtaining for TEM sample preparation using FIB. *Ultramicroscopy* **2020**, *219*, 113135. DOI: https://doi.org/10.1016/j.ultramic.2020.113135.
(25) Ishitani, T.; Umemura, K.; Ohnishi, T.; Yaguchi, T.; Kamino, T. Improvements in performance of focused ion beam cross-sectioning: aspects of ion-sample interaction. *J. Electron Microsc.* **2004**, *53* (5), 443–449. DOI: 10.1093/jmicro/dfh078 (accessed 2/10/2026).
(26) Gillen, G.; Szakal, C.; Brewer, T. M. Useful Yields of Organic Molecules under Dynamic SIMS Cluster Bombardment. *Surf. Interface Anal.* **2011**, *43* (1-2), 376–379. DOI: 10.1002/sia.3484.
(27) Muramoto, S.; Graham, D. J. Deep depth profiling using gas cluster secondary ion mass spectrometry: Micrometer topography development and effects on depth resolution. **2021**, *53* (9), 814–823. DOI: https://doi.org/10.1002/sia.6983.
(28) Barlow, A. J.; Sano, N.; Murdoch, B. J.; Portoles, J. F.; Pigram, P. J.; Cumpson, P. J. Observing the evolution of regular nanostructured indium phosphide after gas cluster ion beam etching. *Appl. Surf. Sci.* **2018**, *459*, 678–685. DOI: https://doi.org/10.1016/j.apsusc.2018.07.195.
(29) Muramoto, S. Towards Pharmaceutical Particle Imaging in Ultrathick Organic Films: 3D Visualization and Image Distortions Using Gas Cluster Bombardment Secondary Ion Mass Spectrometry. *Surf. Interface Anal.* **2025**, *57* (3), 193–202. DOI: https://doi.org/10.1002/sia.7373.
(30) Seah, M. P.; Hunt, C. P. The depth dependence of the depth resolution in composition–depth profiling with Auger Electron Spectroscopy. *Surf. Interface Anal.* **1983**, *5* (1), 33–37. DOI: https://doi.org/10.1002/sia.740050108.
(31) Greer, J. A.; Fenner, D. B.; Hautala, J.; Allen, L. P.; DiFilippo, V.; Toyoda, N.; Yamada, I.; Matsuo, J.; Minami, E.; Katsumata, H. Etching, smoothing, and deposition with gas-cluster ion beam technology. *Surf. Coat. Technol.* **2000**, *133-134*, 273–282. DOI: https://doi.org/10.1016/S0257-8972(00)00876-8.
(32) Sheraz née Rabbani, S.; Berrueta Razo, I.; Kohn, T.; Lockyer, N. P.; Vickerman, J. C. Enhancing Ion Yields in Time-of-Flight-Secondary Ion Mass Spectrometry: A Comparative

Study of Argon and Water Cluster Primary Beams. *Anal. Chem.* **2015**, *87* (4), 2367–2374. DOI: 10.1021/ac504191m.
(33) Breuer, L.; Tian, H.; Wucher, A.; Winograd, N. Molecular SIMS Ionization Probability Studied with Laser Postionization: Influence of the Projectile Cluster. *The Journal of Physical Chemistry C* **2019**, *123* (1), 565–574. DOI: 10.1021/acs.jpcc.8b10245.
(34) Sjövall, P.; Rading, D.; Ray, S.; Yang, L.; Shard, A. G. Sample Cooling or Rotation Improves C60 Organic Depth Profiles of Multilayered Reference Samples: Results from a VAMAS Interlaboratory Study. *J. Phys. Chem. B* **2010**, *114* (2), 769–774. DOI: 10.1021/jp9095216 (accessed 2013/12/17).
(35) Zalar, A. Improved Depth Resolution by Sample Rotation during Auger Electron Spectroscopy Depth Profiling. *Thin Solid Films* **1985**, *124* (3–4), 223–230. DOI: http://dx.doi.org/10.1016/0040-6090(85)90269-X.